Nonlinear and self-consistent single-mode formulation for TM-mode gyrotrons

Hsin-Yu Yao ,[*] Cheng-Hsiung Wei ,[†] and Tsun-Hsu Chang [‡]
Department of Physics, National Tsing Hua University, Hsinchu, 30013, Taiwan

This work develops a nonlinear and self-consistent framework for the single-mode simulation of TM-mode gyrotrons. Unlike TE modes, a nonlinear TM wave equation is derived by considering the additional axial modulation on the electron beam due to the interaction with the axial electric field. Together with the electrons' equations of motion, particle tracing simulation is conducted to model TM-mode oscillation. For a uniform structure, the electron-beam efficiency of the TM_{11}-mode gyrotron at the *W* band can achieve 30% over broad parameter space. Its beam-current, beam-voltage, and pitch-factor tuning properties are investigated under different magnetic fields. By optimizing the interaction structure of the proposed gyrotron backward-wave oscillator (gyro-BWO), the maximum interaction efficiency is higher than 30% with a frequency tuning range of more than 6 GHz at the pitch factor of 1.5. The peak efficiency can remain high of 32% at low beam voltage (10 kV) and low magnetic field (32.8 kG), indicating additional operating conditions. These special features may facilitate the development of low-cost and compact gyrotron systems and show great potential in the applications for TM-mode gyro-BWOs.

I. INTRODUCTION

Gyrotrons have been widely regarded as high-power sources of millimeter and terahertz waves [1–4]. Stimulated cyclotron emission process of energetic electrons in gyrational motion serves as the key mechanism [1,2]. The gyrating electrons possess transverse velocity ($\mathbf{v}_\perp$) and axial velocity ($v_z\mathbf{e_z}$), forming an electric current with a volume current density $\mathbf{J}$. This current can interact with AC electric field ($\mathbf{E} = \mathbf{E}_\perp + E_z\mathbf{e_z}$), and their energy exchanging rate is directly determined by the product of $\mathbf{v}_\perp \cdot \mathbf{E}_\perp + v_zE_z$. Changing the kinetic energy of the electron beam results in the change of relativistic factor (γ) as well as relativistic electron cryotron frequency ($\propto 1/\gamma$), causing the azimuthal bunching [1,2,5]. On the other hand, not only transverse AC magnetic field ($\mathbf{B}_\perp$) but also E_z can modulate the electron's axial velocity v_z through the Lorentz force ($q\mathbf{v}_\perp \times \mathbf{B}_\perp$ and qE_z, respectively), resulting in the axial bunching [1,2,5].

For TE circular-waveguide modes (with $E_z = 0$), the axial bunching can be omitted due to negligible $\mathbf{B}_\perp$ at near-cutoff operation [6]. The azimuthal bunching thus dominates, indicating weak bunching competition and thus high efficiency. For TM-mode gyrotrons, although near-cutoff operation can partially suppress the azimuthal bunching due to the minimized $\mathbf{E}_\perp$, the existence of E_z can still induce both of the bunching processes through the relativistic effect. Traditional understanding usually expects that these two bunching mechanisms always compete [1,5], and severe competition would significantly reduce the interaction efficiency. Besides, both

E_z and $\mathbf{v}_\perp \times \mathbf{B}_\perp$ would modulate v_z of electrons. Although their effects would mutually compensate, the net modulation might still increase the velocity spread and thus reduce the interaction efficiency. Serious bunching competition and severe velocity spread are the two primary reasons that TM modes are unfavorable for the gyrotron community [7–13]. It is worth noting that for the cyclotron autoresonance maser amplifiers operated under highly relativistic and far-cutoff conditions, TM modes are generally considered [13–26] even though both of $\mathbf{E}_\perp$ and $\mathbf{B}_\perp$ are not zero, and the two bunching mechanisms still compete.

However, a more recent study pointed out that the azimuthal bunching and the axial bunching for TM modes can cooperate with each other under the backward-wave operation [7,8]. This finding has also been validated in a more recent work, where the starting behaviors of TM-mode gyrotrons were thoroughly analyzed under small-signal assumption [9,10]. Since the optimal operating condition for TE and TM modes are different [7–10,15], correctly choosing the electron guiding center can effectively reduce (raise) the starting current of the TM_{11} (TE_{01}) mode, facilitating the development of a single TM-mode gyrotron system. Furthermore, a nonlinear but fixed field simulation showed that for backward-wave amplifier, the linear gain and the bandwidth of the TM_{11}-mode gyrotron are as good as those of the TE_{01}-mode gyrotron [9]. Although those previous studies all indicate that the interaction efficiencies of "some" TM modes are as good as those of most TE modes [7–13], those theories were developed either under small-signal (quasilinear) approximation or in non-self-consistent framework. Therefore, there are still many debates about whether a high-power and frequency-tunable TM-mode gyrotron system can be realized.

From the experimental viewpoint, many non-TE oscillations have been observed in the overmoded interaction

---
[*]s5te633v@hotmail.com
[†]wkmicy0204@gmail.com
[‡]Corresponding author: thschang@phys.nthu.edu.tw

structures [27]. Those unidentified peaks might be the evidence of TM-mode oscillations. Besides, 3D particle-in-cell simulations further showed the possibility of high-power TM$_{51}$ and TM$_{71}$ single-mode gyrotrons [28]. To confirm those extraordinary results, a complete theory is required. Although a general form applicable to both TE-mode and TM-mode gyrotrons has been developed in Refs. [16–20], there still lack systematic studies of the behaviors of TM-mode gyrotrons and its underlying beam-wave interaction mechanisms.

This work develops a nonlinear and self-consistent formula for TM-mode gyrotrons. By considering the peculiar interaction term $v_z E_z$ of TM modes, a nonlinear wave equation is derived. The equations of motion of electrons under the interaction of a single TM mode are also calculated for particle tracing simulation. Based on the developed formulas, the nonlinear oscillation behaviors of the TM$_{11}$-mode gyrotron are analyzed under diverse conditions, including beam-current, beam-voltage, pitch-factor, and magnetic-field tunings. Several unique features, such as high feasibility for far-cutoff and backward-wave operation, high stability to beam-parameter tunings, and strong resistance to the velocity spread, are observed and explained. Furthermore, after properly optimizing the radius-taper interaction structure, the maximum beam efficiency can be enhanced to 35% with more than 6-GHz tunable bandwidth. These findings may facilitate the development of low-cost and compact TM-mode gyrotron systems, showing great potential in high-power and frequency-tunable terahertz sources.

II. NONLINEAR AND SELF-CONSISTENT MODEL

The wave equation for an AC electric field **E** driven by charge and current sources can be written as

$$\nabla^2 \mathbf{E} - \frac{1}{c^2}\frac{\partial^2 \mathbf{E}}{\partial t^2} = 4\pi \nabla \rho + \frac{4\pi}{c^2}\frac{\partial \mathbf{J}}{\partial t}, \tag{1}$$

where ρ (**J**) is the volume charge (current) density. The single-mode solution of Eq. (1) can be derived under the assumptions of sufficiently weak mode competition and conversion [29–32]. For a uniform tube with a radius of r_w, the field generating function of a right-hand circularly polarized TM$_{mn}$ mode is

$$E_z = k_{mn}^2 \mathrm{Re}[f(z)J_m(k_{mn}r)e^{i(m\theta - \omega t)}], \tag{2}$$

where $f(z)$ is the axial complex field profile, ω is the angular frequency, $k_z = \sqrt{(\omega/c)^2 - k_{mn}^2}$ is the propagation constant, c is the speed of light in vacuum, and J_m is the Bessel function of the order m. $k_{mn} = x_{mn}/r_w$, where x_{mn} is the nth root of J_m, satisfying $J_m(x_{mn}) = 0$. Based on Eq. (2), the other field components can be derived [6]. Substituting those field components into the z part of Eq. (1), we have

$$\mathrm{Re}\left[k_{mn}^2\left(\frac{\partial^2}{\partial z^2} + k_z^2\right)J_m(k_{mn}r)f(z)e^{i(m\theta - \omega t)}\right]$$
$$= \frac{4\pi}{c^2}\frac{\partial J_z}{\partial t} - i\frac{4\pi}{\omega}\left\{\frac{\partial}{\partial z}\left[\frac{1}{r}\frac{\partial}{\partial r}(rJ_r) + \frac{1}{r}\frac{\partial}{\partial \theta}J_\theta\right] + \frac{\partial^2}{\partial z^2}J_z\right\}. \tag{3}$$

After eliminating the temporal and the transverse spatial dependences of Eq. (3) and converting it to the slowly varying coordinate [32], we have

$$\left(\frac{\partial^2}{\partial z^2} + k_z^2\right)f(z)$$
$$= \left(\frac{8I_b}{\omega x_{mn}^2 K_{mn}}\right)\sum_{j=1}^{N_e}\sum_{s=-\infty}^{\infty} W_j\left[\frac{p_{\perp,j}}{p_{z,j}}\frac{s}{r_{L,j}}\frac{f'^*(z)}{f^*(z)} + ik_{mn}^2\right]$$
$$\times C_{sm}^{1/2}e^{iA_{sm,j}}, \tag{4}$$

where I_b represents the electron beam current, $K_{mn} = J_m'^2(x_{mn})$, $C_{sm}^{1/2} = J_{s-m}(k_{mn}r_{c,j})J_s(k_{mn}r_{L,j})$ is the field coupling strength for TM modes [7–10,15], and $A_{sm,j} = \omega t_j - s\phi_j - (s-m)\psi_j + (m-s/2)\pi$. Hereafter the prime notation represents the first-order derivative of a variable with respect to z, and the asterisk superscript denotes the complex conjugate. The subscript j denotes the quantities of the jth electron, the slowly varying variables of which: W_j (momentum weighting factor), $p_{\perp,j}$ (transverse momentum), $p_{z,j}$ (axial momentum), $r_{c,j}$ (guiding center radius), $r_{L,j}$ (Larmor radius), ϕ_j, and ψ_j are defined in Fig. 1(a) and Ref. [32]. The ratio of $p_\perp(z=0)$ to $p_z(z=0)$ at the beam entrance is defined as the pitch factor α.

Equation (4) also manifests the conservation of energy. It is equivalent to $P'_{\mathrm{net}} + \tilde{P}_{\mathrm{ohm}} = \tilde{P}_{\mathrm{in}}$, where $P_{\mathrm{net}} \propto [f(z)f'^*(z) - f^*(z)f'(z)]$ is the net power flowing along the positive z direction, $\tilde{P}_{\mathrm{ohm}} \propto |f(z)|^2$ means the Ohmic power per unit length dissipated on the waveguide wall, and $\tilde{P}_{\mathrm{in}} \propto \langle \mathbf{J} \cdot \mathbf{E}^* \rangle_t$ is the power per unit length deposited into the AC field by the electrons. In general, in sub-THz to THz regime, both TE and TM modes would suffer from strong Ohmic dissipation. We will further discuss the Ohmic loss of the TM$_{11}$-mode gyrotron in Sec. III.

On the other hand, the trajectory of a single electron is governed by its equation of motion:

$$\frac{d\mathbf{p}}{dt} = -e\mathbf{E}_{\mathrm{tot}} - \frac{e}{c}\frac{\mathbf{p} \times \mathbf{B}_{\mathrm{tot}}}{\gamma m_e}, \tag{5}$$

in which $\mathbf{p} = \mathbf{p}_\perp + p_z\mathbf{e}_z$, m_e denotes the electron's rest mass, and γ is the Lorentz relativistic factor. In Eq. (5), $\mathbf{E}_{\mathrm{tot}}$ is only contributed by the AC field, while $\mathbf{B}_{\mathrm{tot}}$ has an additional contribution from the external DC field [$\mathbf{B}_{\mathrm{ext}} = B_r(r, z)\mathbf{e}_r + B_0(z)\mathbf{e}_z$]. $B_0(z)$ leads to the gyromotion of electron beam, and $B_r(r, z) = -rB_0'(z)/2$, satisfying the paraxial condition. Note that the gyrating electrons corotate with the circularly polarized TM wave. Substituting all the AC-field components into Eq. (5) and following the similar mathematic approaches for deriving Eq. (4), we obtain

$$\frac{dp_\perp}{dz} = \frac{m_e\Omega'_e}{2}[r_L + r_c\sin(\phi - \psi)] + \frac{ek_{mn}}{c}\frac{\gamma m_e c}{p_z}$$
$$\times \mathrm{Re}\left\{\left[-if'(z) - \frac{k_0 p_z}{\gamma m_e c}f(z)\right]\sum_{s=-\infty}^{\infty}\frac{s}{k_{mn}r_L}C_{sm}^{1/2}e^{-iA_{sm}}\right\}, \tag{6}$$
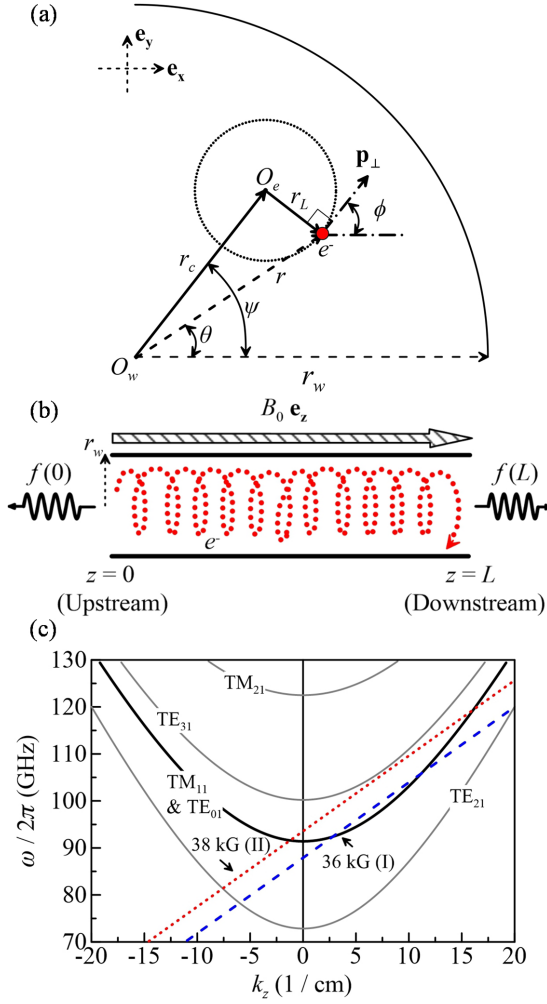
FIG. 1. (a) Schematic of a gyrating electron on the cross section of waveguide. $O_w(O_e)$ denotes the waveguide center (electron guiding center). (b) Schematic of a uniform interaction tube. Only the backward (forward) wave is present at the upstream (downstream) end, corresponding to the outgoing wave boundary conditions. (c) Parabolic curves are the waveguide-mode dispersions of the degenerate TM_{11} and TE_{01} modes and the potential competitors: TE_{21}, TE_{31}, and TM_{21} modes. Oblique curves are the beam-wave resonant conditions for the two representative magnetic fields (red dots: 36 kG and blue dashes: 38 kG). I_b, V_b, and α are 5 A, 70 kV, and 1.0, respectively.

$$\frac{d\phi}{dz} = \frac{m_e \Omega'_e}{2 p_\perp} r_c \cos(\phi - \psi) + \frac{m_e \Omega_e}{p_z} + \frac{e k_{mn}}{c} \frac{\gamma m_e c}{p_z} \frac{1}{p_\perp}$$
$$\times \mathrm{Re}\left\{ \left[f'(z) - i \frac{k_0 p_z}{\gamma m_e c} f(z) \right] \times \sum_{s=-\infty}^{\infty} H_{sm}^{1/2} e^{-iA_{sm}} \right\}, \tag{7}$$

$$\frac{dp_z}{dz} = -\frac{m_e \Omega'_e}{2} \frac{p_\perp}{p_z} [r_L + r_c \sin(\phi - \psi)] + \frac{e k_{mn}}{c} \frac{p_\perp}{p_z}$$
$$\times \mathrm{Re}\left\{ f(z) \sum_{s=-\infty}^{\infty} \left(\frac{s k_0}{k_{mn} r_L} - \frac{\gamma m_e c k_{mn}}{p_\perp} \right) C_{sm}^{1/2} e^{-iA_{sm}} \right\}, \tag{8}$$

TABLE I. Beam parameters.

r_{c0} (mm)	α	I_b (A)	V_b (kV)
0.00	1.0	5	70

$$\frac{dr_c}{dz} = -\frac{\Omega'_e}{2\Omega_e} [r_c - r_L \sin(\phi - \psi)] - \frac{\gamma e k_{mn}}{\Omega_e p_z}$$
$$\times \mathrm{Re}\left[\left\{ \sum_{s=-\infty}^{\infty} \left[i f'(z) + \frac{k_0 p_z}{\gamma m_e c} f(z) \right] \frac{s - m}{k_{mn} r_c} C_{sm}^{1/2} e^{-iA_{sm}} \right\} \right], \tag{9}$$

$$\frac{d\psi}{dz} = -\frac{\Omega'_e}{2\Omega_e} \frac{r_L}{r_c} \cos(\phi - \psi) - \frac{\gamma e k_{mn}}{\Omega_e p_z} \frac{1}{r_c}$$
$$\times \mathrm{Re}\left\{ \sum_{s=-\infty}^{\infty} \left[f'(z) - i \frac{k_0 p_z}{\gamma m_e c} f(z) \right] G_{sm}^{1/2} e^{-iA_{sm}} \right\}, \tag{10}$$

$$\frac{dt}{dz} = \frac{1}{v_z}, \tag{11}$$

where $\Omega_e = eB_0/m_e c$ (electron cyclotron frequency), $k_0 = \omega/c$, $H_{sm}^{1/2} = J_{s-m}(k_{mn} r_c) J'_s(k_{mn} r_L)$ (field coupling strength for TE modes), and $G_{sm}^{1/2} = J'_{s-m}(k_{mn} r_c) J_s(k_{mn} r_L)$. Equations (6)–(8) dominate the dynamic changes of electron momentum, and Eqs. (9) and (10) describe how the electron's guiding center moves under beam-wave interaction.

Equations (4)–(11) together with $f'(z) = df(z)/dz$ form a set of coupled differential equations, which can be jointly solved by integration (e.g., Runge-Kutta method). The obtained $f(z)$ and $f'(z)$ at the collector end (the last z point) are examined by the outgoing-wave boundary condition [10] [Fig. 1(b)] to solve the oscillating frequency (ω_0) and the field amplitude at the injection end [$|f(z = 0)|$]. With the solved $f(z)$, total electron-beam efficiency (η_b), forward-wave efficiency (η_{fwd}), backward-wave efficiency (η_{bwd}), and Ohmic dissipation efficiency (η_{ohm}) can be calculated [32].

III. NONLINEAR TM₁₁-MODE GYROTRON EFFICIENCY IN A UNIFORM TUBE

Properly choosing the initial electron's guiding center radius r_{c0} can enlarge the beam-wave coupling strength of a certain waveguide mode (C_{sm} for TM and H_{sm} for TE), such that the oscillations of unwanted modes can be suppressed. The subscript "0" stands for the initial beam parameter at $z = 0$. Our previous work [10] showed that TM_{11} mode favors $r_{c0} = 0$ (largest coupling coefficient C_{sm}), while this condition is unfavorable for its major competitor—TE_{01}, as well as the nearby competing modes TE_{21} and TE_{31} due to their zero beam-wave coupling strengths $H_{sm} \propto J_{1-m}^2(0) = 0$ with $s = 1$ and $m \neq 1$. Consequently, we fix r_{c0} at 0 (corresponding to an axis-encircling electron beam) to avoid mode competition. Other beam parameters, including the current (I_b), the voltage (V_b), and the pitch factor ($\alpha = p_{\perp 0}/p_{z0} = v_{\perp 0}/v_{z0}$) are listed in Table I. These values will be used in the following analyses unless they are specially specified or tuned. Firstly, we will
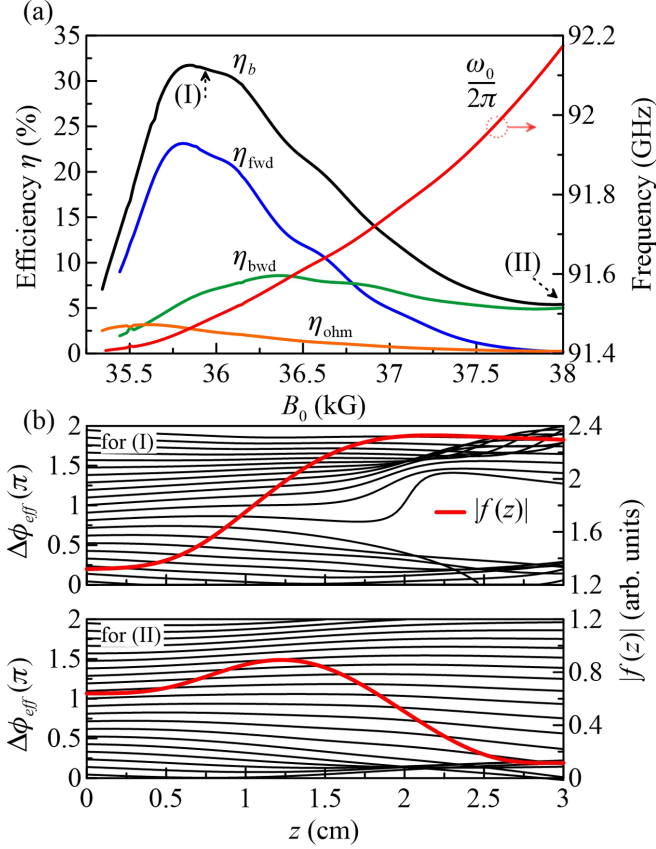
FIG. 2. (a) Nonlinear efficiencies and oscillating frequency vs magnetic field. Color codes: black (electron-beam efficiency, η_b), blue (forward-wave efficiency, η_{fwd}), green (backward-wave efficiency, η_{bwd}), orange (Ohmic dissipation efficiency, η_{ohm}), and red (oscillating frequency, $\omega_0/2\pi$). (b) Electron's effective cyclotron phase-angle change ($\Delta\phi_{\text{eff}}$) and field amplitude profile ($|f(z)|$) vs z. Condition (I) corresponds to the peak efficiency at 36 kG, while condition (II) represents the stable operating region at 38 kG. Top (bottom) panel is for 36 kG (38 kG).

consider a uniform interaction tube [Fig. 1(b)], whose radius (r_w) is selected as 0.2 cm (the TM$_{11}$ cutoff: 91.41 GHz), and the interaction length (L) is 3.0 cm. The tube wall is assumed to be copper with resistivity $\rho_{\text{Cu}} = 1.72 \times 10^{-8}\Omega$ m. An optimized radius-taper interaction structure will be considered in the next section (Sec. IV).

A. Nonlinear efficiencies of TM$_{11}$-mode gyrotron and the underlying physics

Figure 1(c) shows the waveguide-mode dispersions [$\omega^2 - c^2(k_z^2 + k_{mn}^2) = 0$] and the beam-wave resonant lines [$\omega - k_z v_{z0} - s\Omega_{c0} = 0$ ($\Omega_{c0} = eB_0/\gamma_0 m_e c$)] for the uniform tube specified above. We consider only the fundamental harmonic ($s = 1$). Although this plot is restricted to linear regime without beam-wave coupling, it can still qualitatively explain some nonlinear behaviors [1]. Figure 2(a) demonstrates the four nonlinear efficiencies (η_b, η_{fwd}, η_{bwd}, and η_{ohm}), together with the oscillating frequency (ω_0). Maximum electron-beam efficiency ($\eta_b = \eta_{\text{fwd}} + \eta_{\text{bwd}} + \eta_{\text{ohm}}$) achieves 31%, occurring around 36 kG. η_b gradually reduces as B_0 is detuned from the peak-efficiency condition, while ω_0 monotonically de-

creases with the decrease of B_0 until reaching the TM$_{11}$ cutoff (91.41 GHz). At 36 kG (the representative case for peak efficiency) η_{ohm} is 2.34%, implying 28.66% interaction efficiency (the output power divided by the input beam power). The cases with higher metal resistivities were also considered, while the results are not shown in Fig. 2(a) for clarity. When the resistivity increases to $10\rho_{\text{Cu}}$, η_b slightly increases to 31.88%, while η_{ohm} is enhanced to 6.88%. It implies that the interaction efficiency will slightly decrease from 28.66% to 25% due to the stronger dissipation by the waveguide wall.

η_{fwd} is strongly dependent on B_0, while η_{bwd} is relatively stable under the magnetic-field tuning. The "hill shape" of η_b is dominated by the generation of forward wave, while the backward-wave oscillation only adjusts the efficiency baseline. The tendencies of these nonlinear efficiencies, η_{fwd} and η_{bwd}, stem from their beam-wave interacting nature in linear regime. Recall the TM-mode linear efficiency derived in Eq. (7a) of Ref. [7]:

$$\eta_{b,\text{lin}} \propto -\left(v_{z0} - \frac{sk_z}{k_{mn}^2 r_L}v_{\perp 0}\right) \times \left(\frac{v_{z0}}{c}k_0 - k_z\right). \quad (12)$$

The two terms in the first parentheses represent the work done on the electrons by $E_\perp$ and E_z, and the other two terms in the second parentheses correspond to the azimuthal and axial bunching induced by E_z. For the backward wave ($k_z < 0$), when the electrons are at losing-energy phase, both $E_\perp$ and E_z will be simultaneously enhanced. Besides, the azimuthal and the axial bunching keep cooperating with each other. Such cooperation always exists no matter how large (small) $|k_z|$ is, implying that the TM backward wave should exhibit stable efficiency and is suitable for far-cutoff operation. This qualitatively explains why η_{bwd} is flat and why only the backward wave dominates when $B_0 = 38$ kG (far cutoff). For the forward wave ($k_z > 0$), its $E_\perp$ and E_z have opposite effects on the beam-wave energy exchanging process, and the two bunching mechanisms always compete. These competitions become worse for large k_z, indicating that η_{fwd} should be small for far-cutoff operation. On the contrary, small k_z at near cutoff can suppress those competitions, leading to the increase of η_{fwd} at relatively low B_0.

We choose two representative cases at different B_0: (I) 36 kG and (II) 38 kG for the following quantitative discussions. Their beam-wave resonant lines are illustrated in Fig. 1(c). The synchronization for $B_0 = 36$ kG (38 kG) occurs at the forward (backward) wave, such that η_{fwd} (η_{bwd}) majorly dominates the oscillation. To further visualize electron bunching under strong beam-wave interaction, we introduce the effective cyclotron phase-angle change of a single electron ($\Delta\phi_{\text{eff}}$) [1,7]:

$$\Delta\phi_{\text{eff}}(z) = \phi(z) + k_z v_z t - \left(\Omega_{c0}\frac{z}{v_{z0}} + k_z z\right), \quad (13)$$

where ϕ is the transient phase angle solved by Eq. (7), t is solved by Eq. (11) that records the arriving time of the particle at the point z, and the background phase angle in the parentheses relates to the simple gyromotion in the absence of beam-wave interaction. Figure 2(b) demonstrates $\Delta\phi_{\text{eff}}$ of all representative electrons, together with the field amplitude profile $|f(z)|$. In both cases, the electrons tend to bunch at the downstream end. When the forward wave dominates [case

(I)], the major field profile extends to the downstream, but when the backward wave dominates [case (II)], the field concentrates at the upstream due to the nonlinear field contraction [33]. Good matching between the strong field and the electron bunching point implies strong beam-wave interaction, leading to the high nonlinear efficiency (>30%) at 36 kG. On the contrary, the mismatching at 38 kG results in the relatively low efficiency (∼5%) for the backward-wave generation.

B. Tuning analysis: Beam current and magnetic field

Figure 3(a) shows the electron-beam efficiency map (η_b) under the magnetic-field tuning (x axis) and the beam-current tuning (y axis). The upper limit of I_b is chosen at 5 A to avoid potential nonstationary oscillations [34,35]. The larger the injected current, the larger the efficiency before the saturation occurs. At far-cutoff operation [e.g., 38 kG, the green curve in Fig. 3(b)], saturation starts at a low current (1.8 A) because of the nonlinear field contraction of backward wave [33]. Excessive electrons yet to interact with strong field have moved to the downstream end, leading to the quick saturation of efficiency. On the contrary, the major field profile shifts to the downstream end under near-cutoff operation. Since electrons can convectively interact with the growing field, the saturation occurs at a relatively high current [e.g., 2.5 A for 36 kG, the red curve in Fig. 3(b)].

Notice that strong I_b would significantly distort both the mode dispersion and the beam-wave resonant line [9], manifesting strong beam-wave interaction. This causes the high-efficiency lobe in Fig. 3(a) to tilt toward low-B_0 region, responsible for the oscillation around cutoff. The white dots in Fig. 3(a) indicate the sufficiently low-efficiency contour of 0.1%, which is defined as the starting oscillation condition. The extracted starting current (I_{st}) along this low-efficiency contour is plotted as the black dots in Fig. 2(c). The red curve is the linear starting current calculated under the small-signal approximation [10]. A reasonably good agreement between these two results confirms the validity of the present nonlinear and self-consistent theory.

C. Tuning analysis: Pitch factor and magnetic field

The electron-beam efficiency map under the magnetic-field tuning (x axis) with various α (y axis) is demonstrated in Fig. 4(a). Through α optimization, maximum efficiency reaches 34% at $\alpha = 1.17$ and $B_0 = 35.89$ kG. Varying α would alter the slope of the beam-wave resonant line in Fig. 1(c) through changing v_{z0}. The larger the α, the smoother the slope, which guarantees the interception of the mode dispersion and the beam-wave resonant line even at low-B_0 region. It explains why the electron-beam efficiency is still above 15% when $\alpha > 1.2$ and $B_0 < 35.5$ kG [the upper left corner in Fig. 4(a)]. It is interesting that the nonlinear efficiency of the TM_{11} mode quickly increases with α and then saturates after $\alpha \sim 0.9$, whereas the efficiency of most TE modes slowly increases with α without apparent saturation. One can still obtain 15% beam efficiency even when α is below 0.7 for $B_0 = 36$ kG. This suggests that for the TM_{11} mode, smaller α can give similarly high efficiency. The moderate α may reduce the difficulty of the electron gun's design and fabrication.
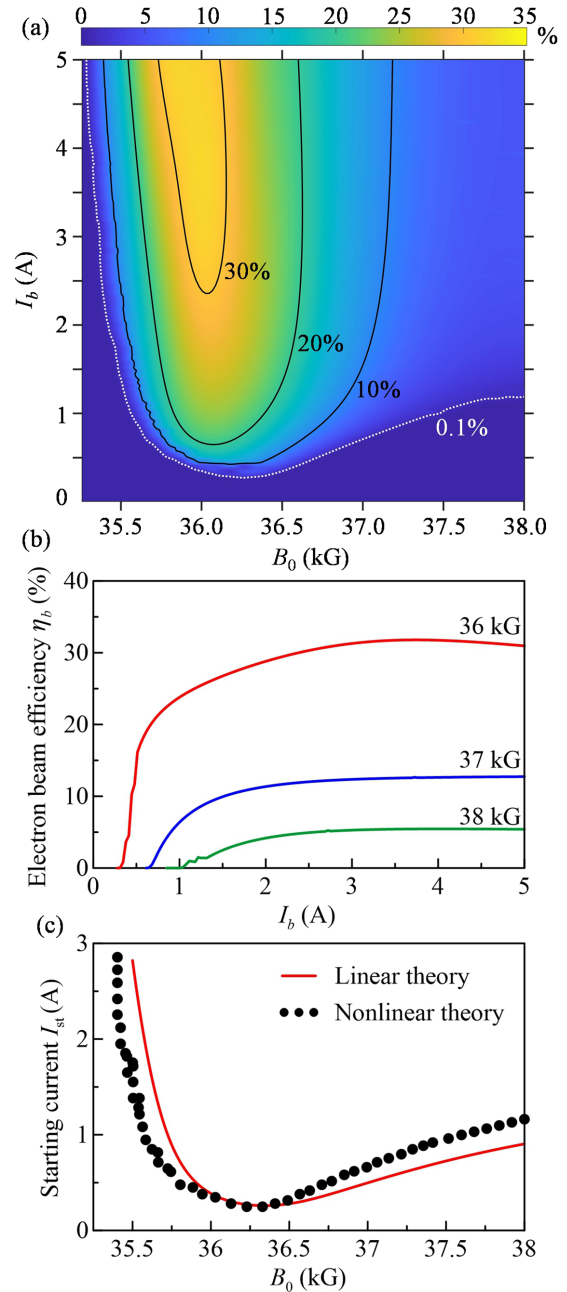

FIG. 3. (a) Electron-beam efficiency map under the magnetic-field tuning (x axis) and the beam-current tuning (y axis). Note that $V_b = 70$ kV and $\alpha = 1.0$. The white dots indicate the contour of $\eta_b = 0.1$%, which is defined as the start-oscillation threshold for the nonlinear simulation. (b) Extracted nonlinear electron-beam efficiency vs beam current for $B_0 = 36$ kG (red, near cutoff), 37 kG (blue), and 38 kG (green, far cutoff). (c) Starting current vs magnetic field. Black dots represent the starting current extracted from (a) along the low-efficiency contour of $\eta_b = 0.1$%. Red curve is the starting current calculated by the small-signal theory developed in Ref. [10].

The saturated behavior of efficiency with respect to α can be understood as follows. As aforementioned, at far-cutoff region, the backward wave leads the oscillation; cooperation occurs between not only $E_\perp$ and E_z, but also the two bunching
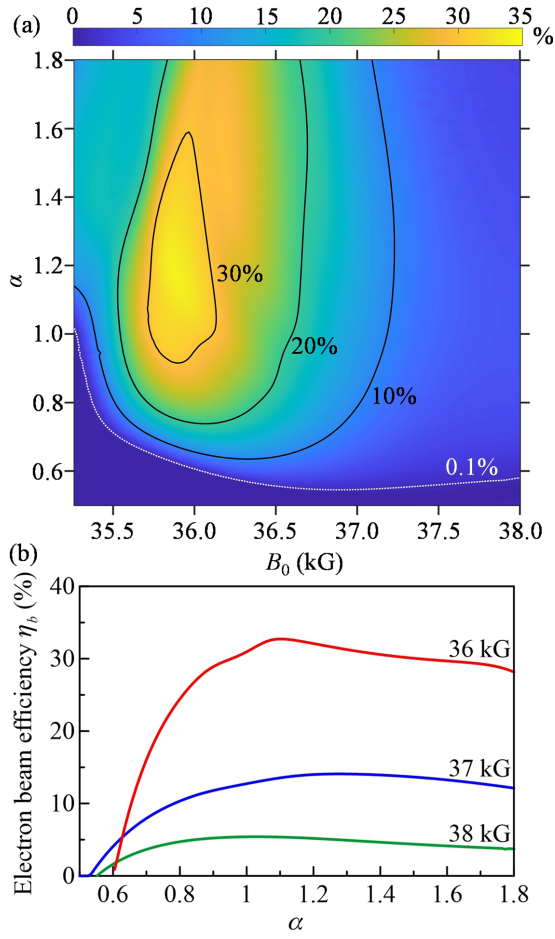
FIG. 4. (a) Electron-beam efficiency map under the magnetic-field tuning (x axis) and the pitch-factor tuning (y axis). Note that $I_b = 5$ A and $V_b = 70$ kV. (b) Extracted nonlinear electron-beam efficiency vs pitch factor for $B_0 = 36$ kG (red, near cutoff), 37 kG (blue), and 38 kG (green, far cutoff).

mechanisms. Since changing α only redistributes $v_{\perp 0}$ and v_{z0}, the balances between the terms in both parentheses in Eq. (12) suggest that η_{bwd} should be insensitive to α. This expectation is confirmed by the green curve in Fig. 4(b) for 38 kG, where $\eta_b \approx \eta_{\text{bwd}}$. On the contrary, once the forward wave dominates, the competition between $E_\perp$ and E_z [the first parentheses in Eq. (12)] becomes worse with the increase of α. Thus, when α is larger than 0.9, severe competition suppresses the forward-wave efficiency, resulting in the saturation and the slight drop of η_b [see the red curve in Fig. 4(b) for 36 GHz].

D. Tuning analysis: Beam voltage and magnetic field

In addition to the magnetic-field tuning, changing the beam voltage (V_b) is an alternative technique to adjust the operating frequency. η_b under the magnetic-field tuning (x axis) and the beam-voltage tuning (y axis) is displayed in Fig. 5. Figure 5(a) shows the tuning results at the high-voltage region (50–100 kV), while the efficiency for the low-voltage tuning (15–30 kV) is in Fig. 5(b). Tuning V_b will simultaneously change the slope and the y-axis intercept of the beam-wave resonant line in Fig. 1(c). The lower the V_b, the lower the
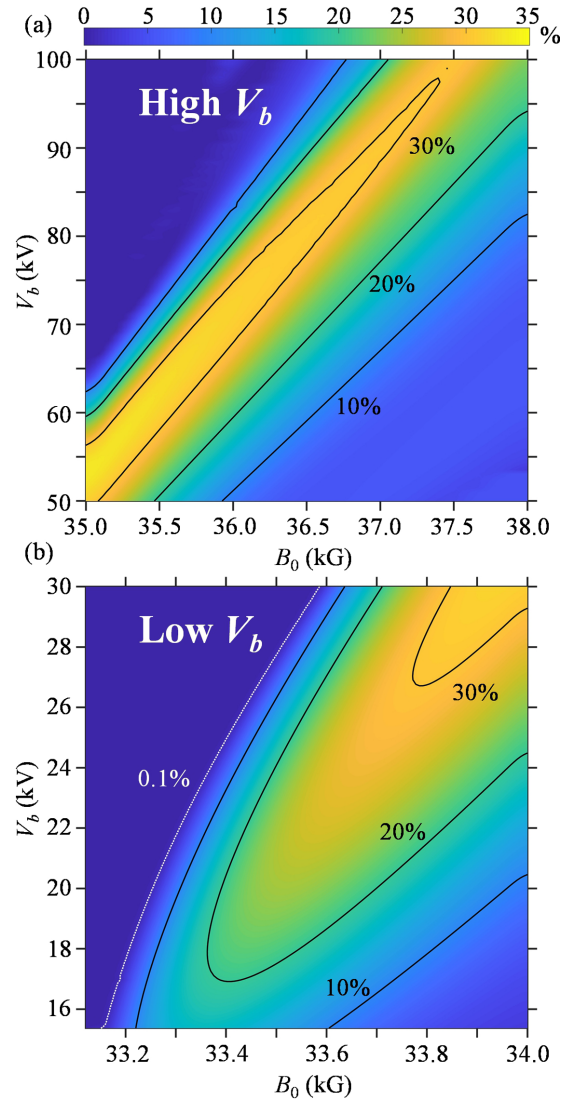

FIG. 5. Electron-beam efficiency map under the magnetic-field tuning (x axis) and the beam-voltage tuning (y axis). (a) High-voltage tuning: 50–100 kV and (b) low-voltage tuning: 15.3–30 kV. Note that $I_b = 5$ A and $\alpha = 1$.

required B_0 for keeping synchronization. The high-efficiency lobe in Fig. 5 thus tilts with the zeroth-order slope of

$$\frac{\Delta V_b}{\Delta B_0} \approx \frac{(511 \text{ kV}) \times e}{\omega_0 m_e c}. \tag{14}$$

We are surprised that the beam efficiency can still be high ($>20\%$) when V_b is reduced to below 20 kV [see the left lower corner of Fig. 5(b)]. This finding suggests that it is possible to realize a low-cost and compact high-power TM-mode gyrotron system operating at low voltage. To operate at even lower voltage (e.g., <10 kV) with similarly high efficiency, further optimization of the interaction structure is necessary. This issue will be addressed in Sec. IV.

E. Sensitivity analysis of velocity spread

Here we analyze the sensitivity of the TM_{11} nonlinear efficiency with respect to the root-mean-square velocity
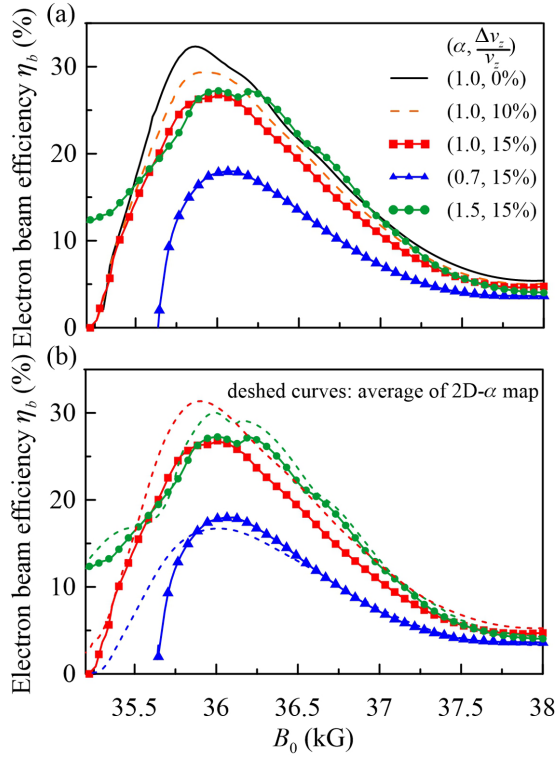
FIG. 6. (a) Nonlinear beam efficiency $\Delta v_z/v_z$ vs magnetic field under different root-mean-square velocity spreads. With $\alpha = 1$, black solid curve, orange dashes, and red squares show the beam efficiencies calculated under the spread of 0, 10, and 15%, respectively. Blue triangles and green circles are, respectively, the beam efficiency for $\alpha = 0.7$ and $\alpha = 1.5$ under a high spread of 15%. (b) Dashes are the theoretical predictions by averaging the efficiency in Fig. 4(a) according to the α spread range evaluated by Eq. (15). Symbols show the efficiencies with diffident α defined in (a).

spread ($\Delta v_z/v_z$). The electron-beam efficiencies under different spread conditions are illustrated in Fig. 6(a). For $\alpha = 1$ (the black solid curve, the orange dashes, and the red squares), η_b at 38 kG almost remains as a constant ($\sim 5\%$) even though the spread has been significantly increased to 15%. Since the backward wave dominates here, the field profile concentrates at the upstream end as shown by the case (II) in Fig. 2(b). It implies that major beam-wave interaction almost completed before the deterioration of electron-beam quality owing to the velocity spread. In other words, the nonlinear field contraction can effectively suppress the spread effect, making the backward wave become more stable. On the other hand, the peak efficiency at 36 kG would slightly reduce as the velocity spread increases from 0 to 15%. As discussed, the peak efficiency is majorly contributed by the oscillation of forward wave. We expect that the forward wave should be relatively sensitive to the spread because of convective beam-wave interaction. It is important to emphasize that even when the spread achieves 15%, the peak efficiency is still as high as 26%; only 6% reduction is observed. This suggests that the TM$_{11}$ mode exhibits good ability to resist the velocity spread.

Regarding the high-spread case ($\Delta v_z/v_z = 15\%$) with $\alpha = 1.5$ [the green dots in Fig. 6(a)], the peak efficiency keeps almost the same as that with $\alpha = 1$. It is not surprising because
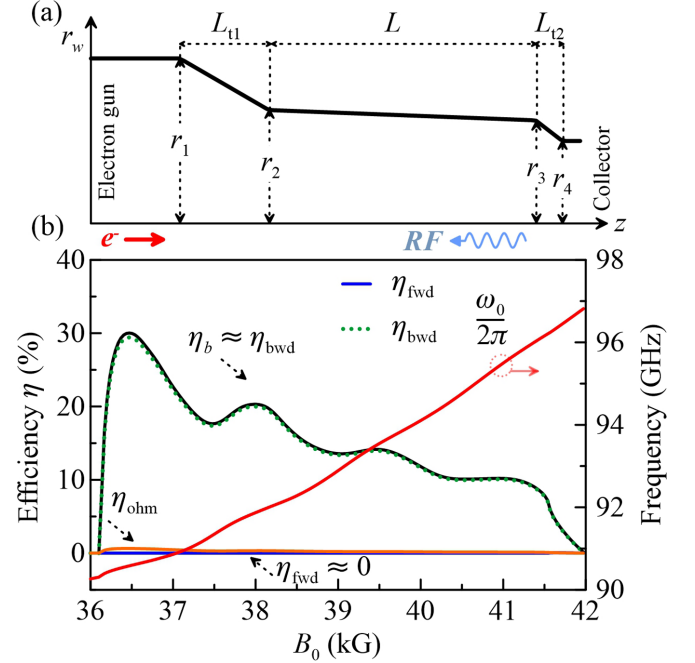

FIG. 7. (a) Geometry of the interaction structure. (b) Nonlinear efficiencies and oscillating frequency vs magnetic field. I_b, V_b, and α are 5 A, 70 kV, and 1.5, respectively. Color codes: black (electron-beam efficiency, η_b), blue (forward-wave efficiency, η_{fwd}), green (backward-wave efficiency, η_{bwd}), orange (Ohmic dissipation efficiency, η_{ohm}), and red (oscillating frequency, $\omega_0/2\pi$).

of the saturation effect after $\alpha > 0.9$. For the high-spread case with a smaller pitch factor [$\alpha = 0.7$, the blue triangles in Fig. 6(a)], the peak efficiency still maintains above 15%. We attribute such strong resistance against the velocity spread to the quick saturation nature of the TM$_{11}$ nonlinear efficiency under α tuning. If the spread is not too high, the energy conservation implies $v_\perp \Delta v_\perp + v_z \Delta v_z \approx 0$. The axial and the transverse velocity spreads are therefore related by $\Delta v_z/v_z \approx -\alpha^2 \Delta v_\perp/v_\perp$. The upper and the lower limits of the possible pitch factor can be written as

$$\alpha_{\pm} \approx \alpha \left[1 \pm \left(\frac{1 + 1/\alpha^2}{1 \mp \Delta v_z/v_z} \right) \frac{\Delta v_z}{v_z} \right]. \quad (15)$$

For $\Delta v_z/v_z = 15\%$, when $\alpha = 0.7$, 1, and 1.5, Eq. (15) predicts that α should range between 0.42–1.07 (spread: 44%), 0.73–1.35 (30%), and 1.21–1.88 (22%), respectively. A large velocity spread would cause an even larger spread of α. It is expected that the efficiency of a case with a certain spread can be evaluated by averaging the efficiency across the aforementioned α spreading range in Fig. 4. The theoretical predictions are plotted in Fig. 6(b) as the dashed curves to compare with the numerical results in symbols. Good qualitative agreement is observed, validating the above physical explanation.

TABLE II. Geometrical parameters (all in mm).

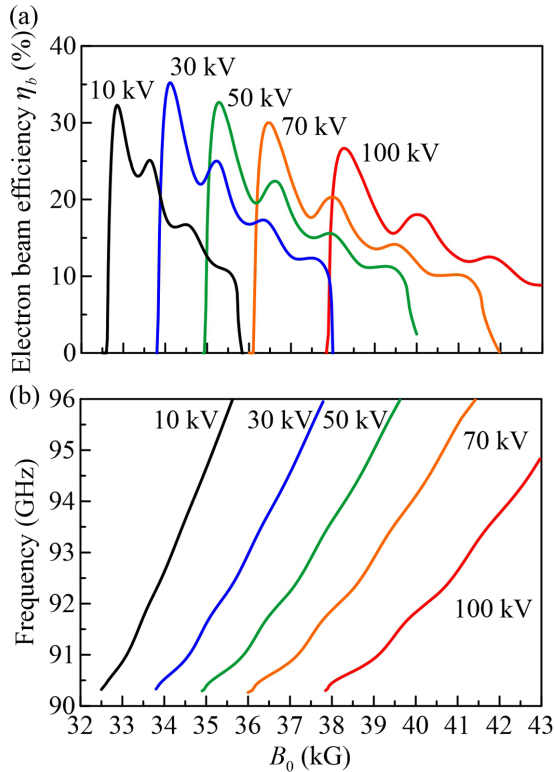| r_1	r_2	r_3	r_4	L_{t1}	L	L_{t2}
2.3	2.05	2.0	1.9	5.0	15.0	1.5

FIG. 8. Nonlinear electron-beam efficiency (a) and oscillating frequency (b) vs magnetic field under different beam voltages. Color codes: red (100 kV), orange (70 kV), green (50 kV), blue (30 kV), and black (10 kV).

In a short summary, those exciting results suggest that some challenging requirements of electron gun, such as high α and low $\Delta v_z/v_z$, can be relaxed. Without those constraints, it is easier to avoid space-charge effect or magnetic-mirroring effect [36,37]. In other words, the difficulty in designing a low-voltage axis-encircling electron gun for the TM_{11}-mode gyrotron can be significantly reduced.

IV. OPTIMIZATION OF THE INTERACTION STRUCTURE

In this section, we consider a more practical case, i.e., an open-cavity structure. Figure 7(a) schematically sketches the optimized structure, the geometrical parameters of which are listed in Table II. There exist two major radius-tapered sections that form a cavity in between. Like most gyro-BWOs [29–31], the beam entrance is opened, and the collector end is shorted by a cutoff. The cutoff reflects all the forward oscillations into the backward wave, which can be extracted using a TM_{11} mode converter [38]. The discrete cutoff junc-

tion may result in mode conversion, and thus the single-mode assumption for deriving Eq. (4) might be violated. Employing a mode-selective circuit is able to overcome this problem [30]; however, it is not the major focus of this work. Figure 7(b) displays the nonlinear efficiencies and the operating frequency with $\alpha = 1.5$ and zero-spread ideal case. As expected, the backward wave contributes to the electron-beam efficiency. The peak efficiency reaches 30% at 36.5 kG. The fractional tuning bandwidth for 5% efficiency achieves 6.39%, ranging from 90.33 to 96.29 GHz. The 3-dB tuning bandwidth is nearly 2 GHz, which is comparable to other TE-mode gyro-BWO systems at *W* band [39]. The effect of the spread is also considered, while the result is not plotted in Fig. 7 for clarity. We find that 15% velocity spread only slightly reduces the peak efficiency by merely 3% and has negligible effect on the oscillating frequency. This result matches the observation in Sec. III E for the uniform interaction tube.

Figures 8(a) and 8(b), respectively, demonstrate the electron-beam efficiency and the oscillation frequency under different beam voltages. The peak η_b slightly increases with the decrease of V_b from 100 to 30 kV. When the voltage is as low as 10 kV, the peak efficiency can still be higher than 30% with a broad tuning bandwidth of 6 GHz and a relatively low magnetic-field requirement.

V. CONCLUSIONS

A nonlinear and self-consistent single-mode theory is developed to study the TM-mode gyrotron oscillators. Extensive operating conditions are simulated, including various beam currents, beam voltages, magnetic fields, pitch factors, and velocity spreads. The simulations find that TM-mode gyrotrons favor backward-wave interaction, which verifies the expectation and the understanding from the linear theories. The backward wave exhibits very stable efficiency and is suitable for relatively far-cutoff operation due to the cooperation of the azimuthal and the axial bunching. We discover that the TM_{11}-mode gyrotron exhibits not only high applicability for far-cutoff and low-voltage operation but also high stability to beam-parameter tuning and velocity spread. Furthermore, with proper optimization of the radius-taper structure, the maximum efficiency of TM_{11} mode can be enhanced to 35% with about 6-GHz tunable bandwidth. Those discoveries and designs may facilitate the development of low-cost and compact TM-mode gyrotron systems to generate high-power and frequency-tunable terahertz signal.

[1] K. R. Chu, Rev. Mod. Phys. **76**, 489 (2004).

[2] G. S. Nusinovich, *Introduction to the Physics of Gyrotrons* (JHU Press, Baltimore, MD, 2004).

[3] M. Thumm, J. Infrared Millimeter, Terahertz Waves **41**, 1 (2020).

[4] G. S. Nusinovich, M. K. Thumm, and M. I. Petelin, J. Infrared, Millimeter, Terahertz Waves **35**, 325 (2014).

[5] K. R. Chu and J. L. Hirshfield, Phys. Fluids **21**, 461 (1978).

[6] D. M. Pozar, *Microwave Engineering*, 3rd ed. (John Wiley & Sons, Inc., Hoboken, NJ, 2006).

[7] T. H. Chang, W. C. Huang, H. Y. Yao, C. L. Hung, W. C. Chen, and B. Y. Su, Phys. Plasmas **24**, 023302 (2017).

[8] T. H. Chang, H. Y. Yao, B. Y. Su, W. C. Huang, and B. Y. Wei, Phys. Plasmas **24**, 122109 (2017).

[9] T. H. Chang and K. J. Xu, Phys. Plasmas **25**, 112109 (2018).

[10] H. Y. Yao, C. C. Chen, and T. H. Chang, Phys. Plasmas **27**, 022113 (2020).

[11] V. L. Bratman, Elektron. Tekh., Ser. I, Elektronika SVCH, 92 (1974).

[12] I. E. Botvinnik, V. L. Bratman, G. G. Denisov, and M. M. Ofitserov, Pis'ma Zh. Tekh. Fiz. **10**, 792 (1984) [Sov. Tech. Phys. Lett. **10**, 332 (1984)].

[13] E. Ott and W. M. Manheimer, IEEE Trans. Plasma Sci. **3**, 1 (1975).

[14] G. Dohler and D. Gallagher, IEEE Trans. Electron Devices **35**, 1730 (1988).

[15] C. Jiao and J. Luo, Phys. Plasmas **13**, 073104 (2006).

[16] N. S. Ginzburg and G. S. Nusinovich, Radiophys. Quantum Electron. **22**, 522 (1979).

[17] N. S. Ginzburg and G. S. Nusinovich, Izu. VUZov Radiofizika **22**, 754 (1979).

[18] V. L. Bratman, N. S. Ginzburg, G. S. Nusinovich, M. I. Petelin, and P. S. Strelkov, Int. J. Electron. **51**, 541 (1981).

[19] V. L. Bratman, G. G. Denisov, M. M. Ofitserov, S. D. Korovin, S. D. Polevin, and V. V. Rostov, IEEE Trans. Plasma Sci. **15**, 2 (1987).

[20] É. B. Abubakirov, Radiophys. Quantum Electron. **26**, 379 (1983).

[21] G. S. Nusinovich and M. Walter, Phys. Plasmas **4**, 3394 (1997).

[22] A. W. Fliflet, Int. J. Electron. **61**, 1049 (1986).

[23] L. Chen, T. H. Kho, and A. T. Lin, Int. J. Infrared, Millimeter Waves **11**, 821 (1990).

[24] S. Sabchevski and T. Idehara, Int. J. Infrared, Millimeter Waves **26**, 669 (2005).

[25] N. Yang and S.-C. Zhang, J. Infrared, Millimeter, Terahertz Waves **30**, 328 (2009).

[26] S. C. Zhang and M. Thumm, Phys. Lett. A **374**, 1745 (2010).

[27] T. Idehara, J. C. Mudiganti, L. Agusu, T. Kanemaki, I. Ogawa, T. Fujiwara, Y. Matsuki, and K. Ueda, J. Infrared, Millimeter, Terahertz Waves **33**, 724 (2012).

[28] A. N. Leontyev, E. B. Abubakirov, V. I. Belousov, Y. M. Guznov, R. M. Rozental, A. E. Fedotov, and V. P. Tarakanov, Bull. Russ. Acad. Sci.: Phys. **84**, 66 (2020).

[29] C. T. Fan, T. H. Chang, K. F. Pao, K. R. Chu, and S. H. Chen, Phys. Plasmas **14**, 093102 (2007).

[30] N. C. Chen, C. F. Yu, C. P. Yuan, and T. H. Chang, Appl. Phys. Lett. **94**, 101501 (2009).

[31] T. H. Chang, T. Idehara, I. Ogawa, L. Agusu, and S. Kobayashi, J. Appl. Phys. **105**, 063304 (2009).

[32] K. R. Chu, H.-Y. Chen, C.-L. Hung, T.-H. Chang, L. R. Barnett, S.-H. Chen, T.-T. Yang, and D. J. Dialetis, IEEE Trans. Plasma Sci. **27**, 391 (1999).

[33] S. H. Chen, K. R. Chu, and T. H. Chang, Phys. Rev. Lett. **85**, 2633 (2000).

[34] T. H. Chang, S. H. Chen, L. R. Barnett, and K. R. Chu, Phys. Rev. Lett. **87**, 064802 (2001).

[35] S. H. Chen, T. H. Chang, K. F. Pao, C. T. Fan, and K. R. Chu, Phys. Rev. Lett. **89**, 268303 (2002).

[36] C. H. Du, T. H. Chang, P. K. Liu, C. P. Yuan, S. J. Yu, G. F. Liu, V. L. Bratman, M. Y. Glyavin, and Y. K. Kalynov, IEEE Trans. Electron Devices **59**, 3635 (2012).

[37] C. H. Tsai, T. H. Chang, Y. Tatematsu, Y. Yamaguchi, M. Fukunari, T. Saito, and T. Idehara, IEEE Trans. Electron Devices **68**, 324 (2020).

[38] H. W. Chao, R. J. Huang, Y. C. Li, and T. H. Chang, Rev. Sci. Instrum. **92**, 053540 (2021).

[39] T. H. Chang, C. F. Yu, C. L. Hung, Y. S. Yeh, M. C. Hsiao, and Y. Y. Shin, Phys. Plasmas **15**, 073105 (2008).